Lattice material infiltration for hybrid metal-composite joints: Manufacturing and static strenght

Lattice material infiltration for hybrid metal-composite joints: manufacturing and static strenght

Luca Raimondi[a*], Luca Tomesani[a,b], Lorenzo Donati[a,b], Andrea Zucchelli[a,b]

[a]*DIN – Università di Bologna, Viale Risorgimento 2, 40136 Bologna, Italia*

[b]*CIRI-MAM – Università di Bologna, Viale Risorgimento 2, 40136 Bologna, Italia*

Corresponding author.
Tel.: +39 393 0555860
E-mail address: luca.raimondi@unibo.it

Abstract

An innovative technological solution for the manufacturing of high strength and high toughness metal-composite interface is here investigated, in which a 3DP printed cellular structure at the metal side is infiltrated by Advanced Sheet Molding Compound composite, in order to understand the effect of main geometric and processing parameters. Some hybrid metal-composite joints were produced, in which the effect of fiber orientation and cell dimension were considered as representative of the main processing issues. The outcome of the infiltration process was first checked on the hybrid joints, then samples were extracted for mechanical characterization of the bond, in comparison with cellular structure free joints.

Keywords:

Hybrid metal-composite joints; Prepreg Compression Molding; Lattice reinforcements; Experiment;

1. Introduction

The growing request for lightweight applications, especially for structural parts in the transportation and automotive industry, raises the need to develop innovative technological solutions for multi-material components, in which different functions are deployed in different regions by the best material for a specific need [1,2]. As an example, metal inserts can be introduced into a composite part in order to allow subsequent assembly operations. The tailoring of different materials within the same component is further enhanced as more weight can be saved by integrating multiple functions in the same component, leading to complex hybrid material solutions [3,4].

In this context, carbon fiber reinforced plastics (CFRP) are mostly used for their extreme stiffness to weight ratio and for the tailoring of the mechanical proprieties through specific layups, whereas metals are selected for their toughness, shock absorption ability, ease to be precisely cut and finished in view of assembly operations. The metal-composite interface has thus from a long time grown as an important issue for high value-added components [5].

The most widely used technique for joining such an interface is the adoption of the adhesive joint. The effects of adopting different material combinations over the strength of the joint have been recently studied both numerically and experimentally, and an extensive literature exists on the topic [6–13]. To obtain a strong and durable joint, a surface treatment of the adherends is required to remove contaminants like lubricants, dust, loose corrosion layers, micro-organisms from the surfaces [14–17] and different physical and chemical surface treatment are available. However, at the industrial scale, they can be difficult to be implemented or will increase the overall production cost for material and time losses.

In order to enhance overall resistance of the bond toughness, in particular, in aerospace applications, the direct insertion of metal protrusions into the composite fabric has been used; protrusions are obtained at high cost by machining directly bulk metal parts [18] or shaped onto the metallic adherend by Electron Beam Melting or Laser Beam Welding [19–21]. Likewise, the penetrative reinforcing technique was used to link different fiber textiles by double-side pin insert extracted from a metal sheet by laser cutting [22,23].

More recently, the fast technological evolution in manufacturing has led, in the field of composites, to composite materials for high production rates, such as Advanced Sheet Molding Compound (ASMC) with short to medium fiber length; these materials can be compression molded into any kind of shape by warm tooling in a short production time [2]. The availability of ASMCs with good mechanical properties, either with thermoset or thermoplastic matrices [24,25], makes their adoption a viable solution for stiffness driven structural applications.

At the same time, in the field of metals, the additive manufacturing technique of selective laser melting (SLM) has led to the production of full density components in which very complex freeform shapes can be obtained at a relatively low manufacturing cost if compared to machining from the bulk. The continuous decrease of costs and the

recent development of in-situ, in-process quality assurance methods [26–28] make SLM a suitable process for the manufacturing of metal inserts for hybrid material components.

In fact, by using SLM, the metal insert can be structured with an inner bulk core and an outer high complex surface where several ASMC tows can penetrate to realize a high strength and high toughness permanent bond [29]. This joining by infiltration can be performed by locating SLM inserts directly in the shape mold where the ASMC material is processed.

The infiltration process will be dependent on several key factors, related to both the ASMC material and the 3DP structure. Due to the engineered properties of the material on the SMC side, the overall fiber orientation [30], the strand length [24], the fiber/matrix volume ratio [25,31], the matrix viscosity as a function of pressure, temperature and time [32–34], should have an impact to the lattice infiltration. On the 3DP structure side, the geometry of the structure [35], the dimension of the cells, their distribution, the void to volume ratio (the density) [36,37], will also have a potential influence on the infiltration.

In this paper, the possibility to infiltrate a 3DP pyramidal cellular structure by SMC sheets in a one-step molding operation is experimentally evaluated, in order to understand the effect of some geometric and processing parameters. Several hybrid metal-composite joints with a complex interface were produced, in which both the effect of fiber orientation and the cell dimension were considered as representative of the main processing issues. The different configuration of two process parameters was then used for two distinct experiments: the first aimed at evaluating the infiltration process, the second for producing samples for mechanical characterization.

2. Materials and Methods

2.1. Metal side

The SLM process was used to directly build the metallic adherend from AISI 316L onto the cylindrical platform of the machine (SISMA MYSINT100) with 99 mm in diameter. The chamber was preliminarily filled with argon to avoid oxidation of the component during the manufacturing process, with a residual oxygen content below 0.2%. An LPW 316 powder was used for manufacturing (LPW Technology Ltd,

Runcorn, UK). Printing parameters were: 150W laser power, 50μm spot diameter 20μm layer thickness as suggested by [38] for higher density.

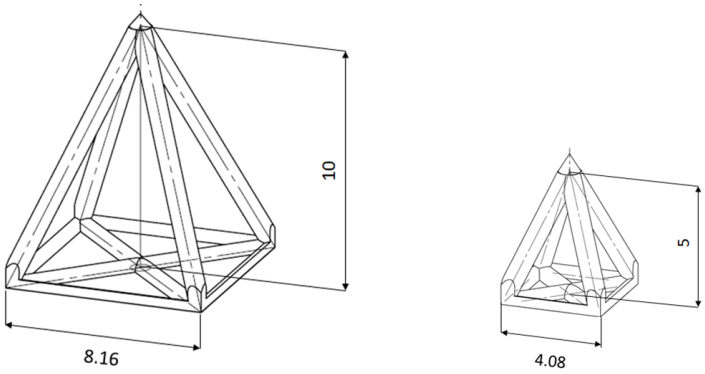

Figure 1: Two types of pyramids: a) big; b) small

The lattice structure which was chosen, among the available in literature, was the pyramidal one. The pyramidal structures was chosen because of its intrinsic high compressive stiffness thanks to stretch dominant behavior [37,39], due to its high efficiency in heat transfer [40–42] and, last but not least, due to the expected effect promoting the SMC charge flow during the moulding process. For the purpose of this study, two dimensions of square-based pyramids were printed: a big one with 8.16 mm side and 10 mm height and a small one with a 4.08 mm side and 5 mm height. For both, rod diameter was 0.80 mm, see Figure 1. Dimensions of pyramids and of rods, were chosen as a compromise between density of the structures, the accuracy obtainable with the 3D printing machine used in this work. The two types of pyramids were printed onto three different types of platform:

- Platform A, with a grid of 86 adjacent elements with 8.16 mm base side (Figure 2. a)
- Platform B, with a grid of 368 adjacent elements with 4.08 mm base side (Figure 2.b)
- Platform C, with a mix of separate elements for samples extraction (Figure 2.c)
    - 4 elements with one big pyramid each (BS, Figure 2 d)
    - 4 elements with 4 small pyramids each (SS, Figure 2 d)
    - 4 elements with flat surface for simple adhesion reference samples (FS, Figure 2 d)

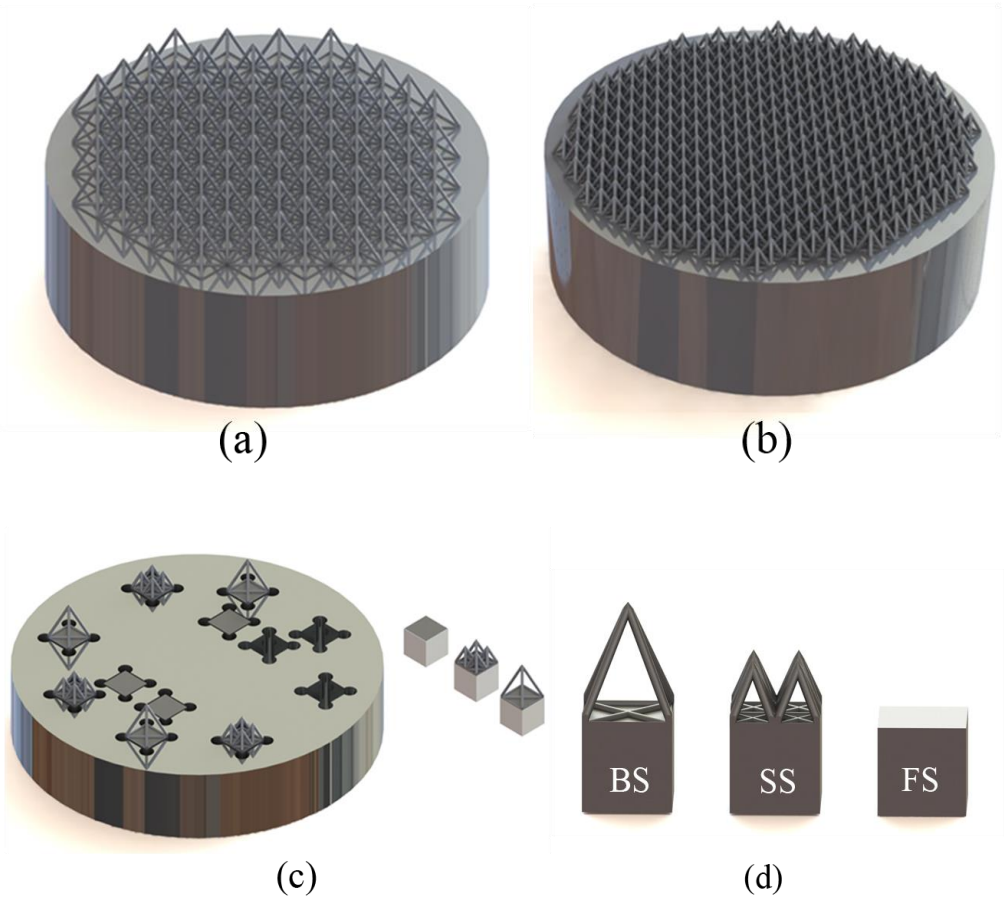

Figure 2: 3D printed grids on platform a) Platform A with a grid of big pyramids b) Platform B with a grid of small pyramids; c) Platform C for extraction of samples for material characterization d) metal adherends for mechanical characterization.

After printing, all the grids were visually checked for imperfections. Care was taken in identifying an appropriate positioning of each grid over the platforms, either to reduce edge effects during infiltration and to cover the largest possible area. In Platform C the supporting elements of the pyramids were covered with a release film (PTFE) in order to ease samples extraction after the molding procedure.

2.2. Composite side

To produce the composite adherend, an HexMC®/C/2000/M77 ASMC supplied by Hexcel, Duxford (UK) was used. Such a material is a carbon fiber prepreg (57% fibre volume fraction, Vf), formed by randomly distributed 50 mm long 8 mm wide chips, with an areal density of 2000 g/m^2 (approximate, as supplied) impregnated with M77 epoxy resin. M77 is a fast curing epoxy (3 min at 140 °C) specifically developed for compression molding.

To investigate the effect of prepreg orientation over processability, two plies orientation within the charge were adopted: (a) parallel to the grid interface and (b) orthogonal to the grid interface.

ASMC roll was extracted from cold storage 4 hours before cutting and put in a white chamber. To obtain the charge for condition (a), 10 circular layers of ASMC of 95 mm diameter were cut out and carefully stacked on top of each other to form a charge of 35 mm in height, as shown in Figure 3a; to obtain the charge for the condition (b), 35 mm width stripes of ASMC were cut using a sharp knife, then wound to form rolls with an average diameter of 95 mm, as shown in Figure 3b.

(a) (b)

Figure 3: a) ASMC stacked with fiber orientation parallel to the platform interface; b) ASMC stacked with fiber orientation orthogonal to the platform interface.

2.3. Compression Molding

Eight different hybrid joints, four for infiltration evaluation and four for mechanical properties evaluation, were manufactured by co-curing the two ASMC stacks towards the three platforms in a custom AISI 316L mold, as shown in Figure 4 a-c and installed into an upstroke laboratory press. The whole experimental plan is depicted in Table 1.

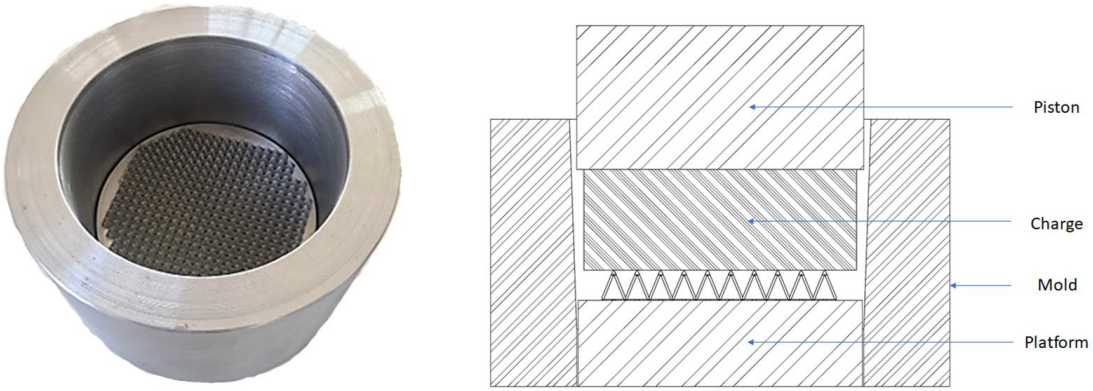

(a) (b)

Figure 4: a) Platform placed at the bottom of the mold b) pressing section

To ensure a uniform temperature distribution, both mold and 3D printed samples were uniformly preheated in an oven at a temperature of 150 °C and monitored by k-type thermocouples with a tolerance of ±2 °C.

***Table 1**: Experimental Plan*

Type of Experiment	Number of molds produced	Platform Type	ASMC Orientation	Samples Produced
Infiltration	1	A	═	n.1 platform for visual inspection
	1	B	═	n.1 platform for visual inspection
	1	A	⊥	n.1 platform for visual inspection
	1	B	⊥	n.1 platform for visual inspection
Mechanical properties/evaluation of samples deformation after curing	2	C	═	n.8 samples BS (Big) n.8 samples SS (Small) n.8 samples FS (Flat)
	2	C	⊥	n.8 samples BS (Big) n.8 samples SS (Small) n.8 samples FS (Flat)

Care was taken in optimizing the compression molding force in order to avoid the possibility of pyramids collapsing. For this purpose, a compression test was performed

on both platforms A and B, as reported in section S1 of supplementary information. As a result of this test, a maximum force of 24 kN was assumed for processing.

The temperature of the plates was set to 150 °C. Metal samples were assembled into the mold, prepreg was charged, and compression-molded, as shown in Figure 4 c for 4 minutes.

2.4. Infiltration evaluation

After curing, the type A and B hybrid joints aimed at infiltration evaluation were progressively milled orthogonally to the interface and visually checked, to put in evidence the presence of unfilled volumes and tow orientation.

2.5. Mechanical testing and data analysis methodology

After curing, the type C hybrid joint was cut into 24 square samples of 13 mm side, using a high-speed rotating diamond tool. Two types of samples were obtained, one with a single embedded pyramid with 8 mm side, the other with four adjacent embedded pyramids with 4mm side each; one more type of flat sample was produced as a reference for the conventional co-curing joining technique. The number of samples produced is reported in Table 1.

Hybrid samples were monotonically loaded at a rate of 0.5 mm/min into an INSTRON 8033 universal testing machine equipped with a 2 kN and a 25 kN load cell, using the custom setup of Figure 5.

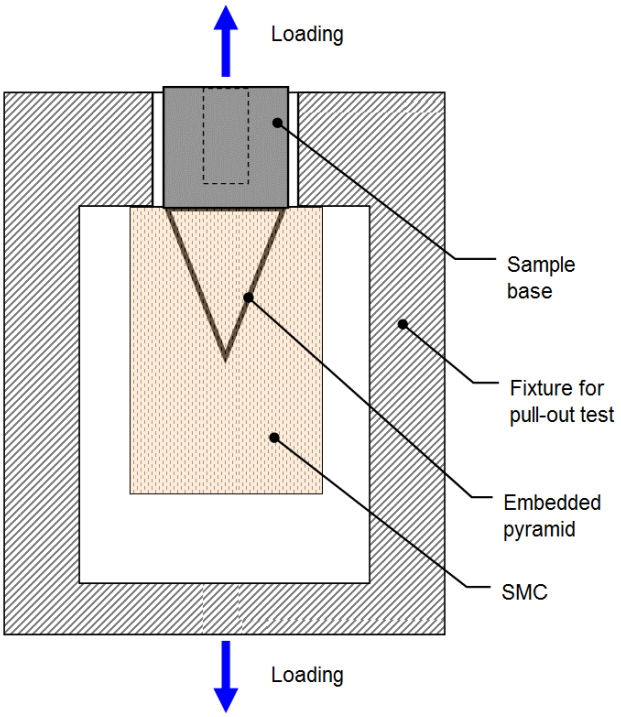

Figure 5: scheme of the testing fixture for pullout test and sample assembly

For each sample, composite adherends were linked to the hydraulic cylinder through a custom fixture with a 9 mm square hole on the top and aligned to the testing machine axis. The base of the metal adherend was connected to the load cell through a spherical connection using a threaded and a cylindrical joining, to prevent misalignment between the sample axis and the testing machine axis under loading. Load and displacement were recorded along the whole pullout test to evaluate load bearing capacity and the absorbed energy of each sample configuration.

In order to concentrate the analysis exclusively on the elasto-plastic behavior of the samples, thus excluding the elastic response of the testing equipment, corrected pullout displacement s was obtained by:

$$s = s_c - \frac{F}{K^*} \qquad (1)$$

where s_c is the measured displacement of the cylinder, F is the opening traction load, and K^* is the stiffness of the load train, which was estimated by a tensile test on a dummy AISI 316L specimen tested with the same equipment.

The failure energy E was calculated as the area under the traction load versus the sample displacement:

$$E = \int F ds \qquad (2)$$

2.6. Analysis of the fractured surface and Morphological characterization

After the pullout test, fractured surfaces of the samples were preliminary analyzed using a ZEISS Stemi 508 Greenough Stereo Microscope equipped with a 5MP ZEISS Axiocam 105 color camera to investigate for their macroscopic failure behavior. Analysis of morphological fracture modes was assessed via Scanning Electron Microscopy (SEM, Phenom ProX). When necessary (e.g. CFRP samples or samples fully covered by resin) analyzed surfaces were gold coated in order to make them conductive.

3. Results and discussion

3.1. Infiltration evaluation

In Figure 6 and Figure 7 the sequence of sections of the hybrid joints in which the prepreg tows were oriented parallel to the interface is presented. In Figure 6, where the grid was made of big pyramids, the ASMC was not able to reach the base of the adherend other than very near to the mold wall, generally stopping in the space between adjacent pyramids. As shown in Figure 6 b and Figure 6 c, excess of resin was identified within the grid in the form of large resin blocks.

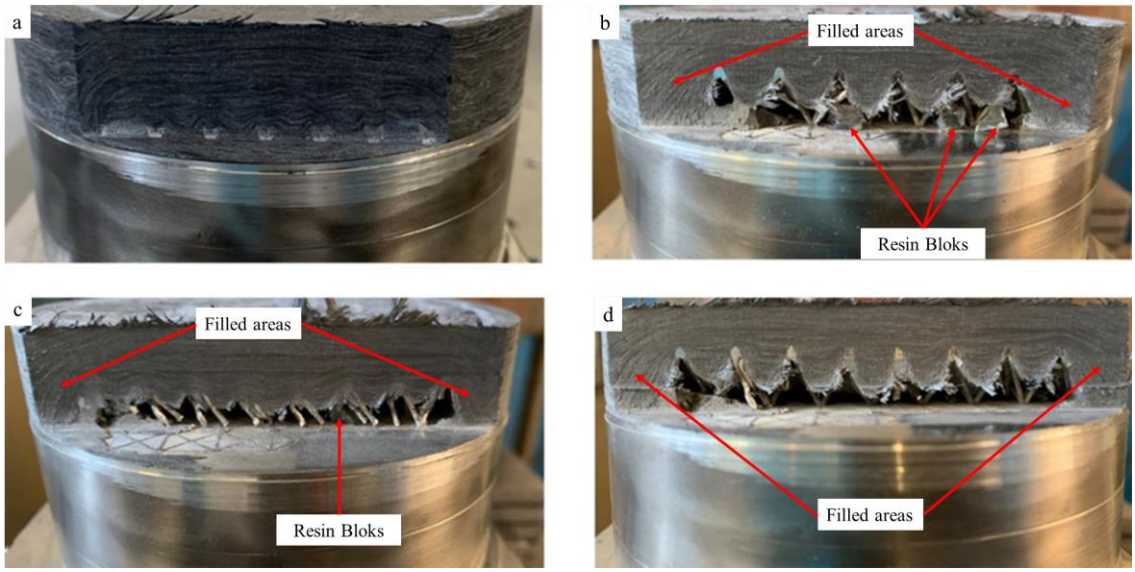

Figure 6: Infiltration results for Platform A (rough grid) - ASMC parallel to the interface

In Figure 7, where the fine grid was used, the resin of the ASMC could somewhere penetrate the lattice up to its base, especially in proximity to the mold wall, but still with vast unfilled areas see Figure 7 b, Figure 7 c and Figure 7 d. The reason for the easier filling near the mold wall may be related to the more efficient heating of the SMC material at the direct contact with the heated mold, whereas the material at the center of the joint could not be perfectly heated by the lattice, as the contact is limited to the vertices of the pyramids. It can be argued that the rough grid lattice, with a reduced number of heating vertices, was much less effective in prepreg heating than the fine grid lattice, where a far larger number of heating points was present. Thus, a complete embedding of the lattice structure by the ASMC material was not successful for both configurations, with the fiber material generally draping around the vertices of the pyramids.

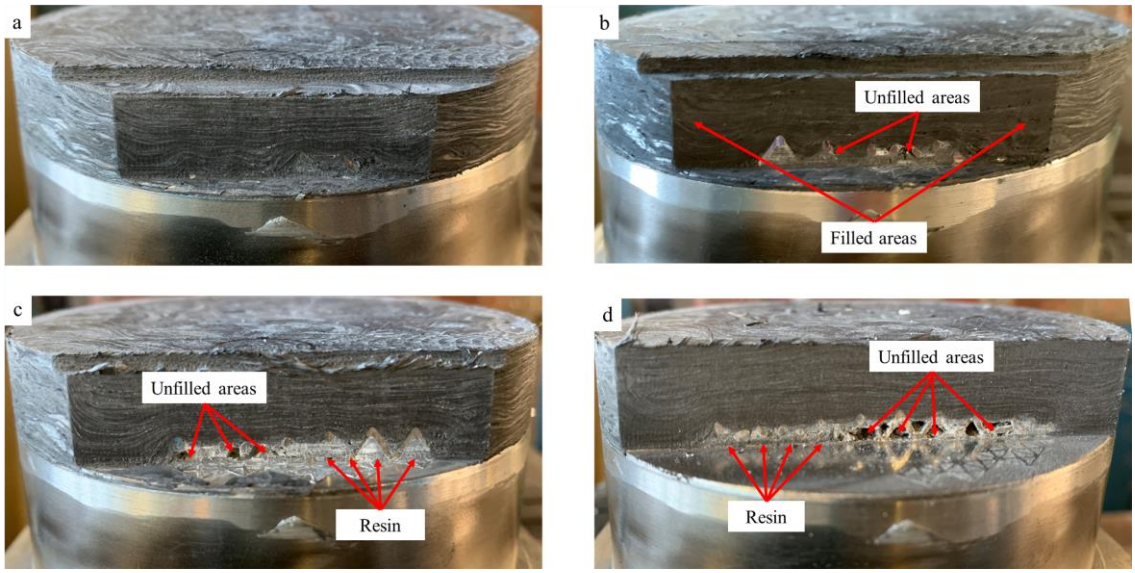

Figure 7: Infiltration results for Platform B (fine grid) - ASMC parallel to the interface

About the general resistance of the lattices to processing flow, no appreciable plastic collapse of the structure was evidenced in both lattice structures in Figure 6 and Figure 7. This result shows that for this particular configuration, the interaction effects over the metal rods of the grid due to the motion of the ASMC during molding can be neglected. Processing force can be therefore adjusted up to the proportionality limit of the lattice material in compression to avoid appreciable plastic deformations on the metal part of the component.

In Figure 8 and Figure 9, the sequence of sections of the hybrid joints, with prepreg tows oriented orthogonally to the interface, is presented. In Figure 8, where the grid was made of big pyramids, the ASMC was able to reach the base of the grid structure at any point of the interface, in particular also in the billet center, although some very clear plastic collapses of the pyramids can be seen at different locations. Such a behavior is related to the infiltration process. In fact during resin infiltration pyramids are compressed at their vertices, and lateral sides are bent since the ASMC flow is forced to fill their volume.

On the other hand, no collapse of the small pyramids was found (Figure 9). It can be stated, then, that complete embedding of pyramidal lattice material was feasible for both configurations in which the charge-constituting SMC tows were oriented orthogonally to the interface (thus aligned with the main molding flow direction), but only the fine grid structure could properly withstand the processing load.

Differently from what happened in the parallel configuration experiments, in the bulk of the ASMC material, diffuse wrinkling in strands is evidenced in all sections of both configurations, as a result of intense fiber displacement and consequent tow buckling. In particular, in Figure 8, where the rough grid lattice is shown, fiber distribution is highly irregular and both tows swirling, and wrinkling can be noticed, as a consequence of the higher displacement to be performed during the molding and, probably, also of the simultaneous buckling of the pyramids. As contrast to that, in Figure 9, the grid configuration with fine grid structure evidences a less severe and almost symmetrical wrinkling distribution about the central vertical axis.

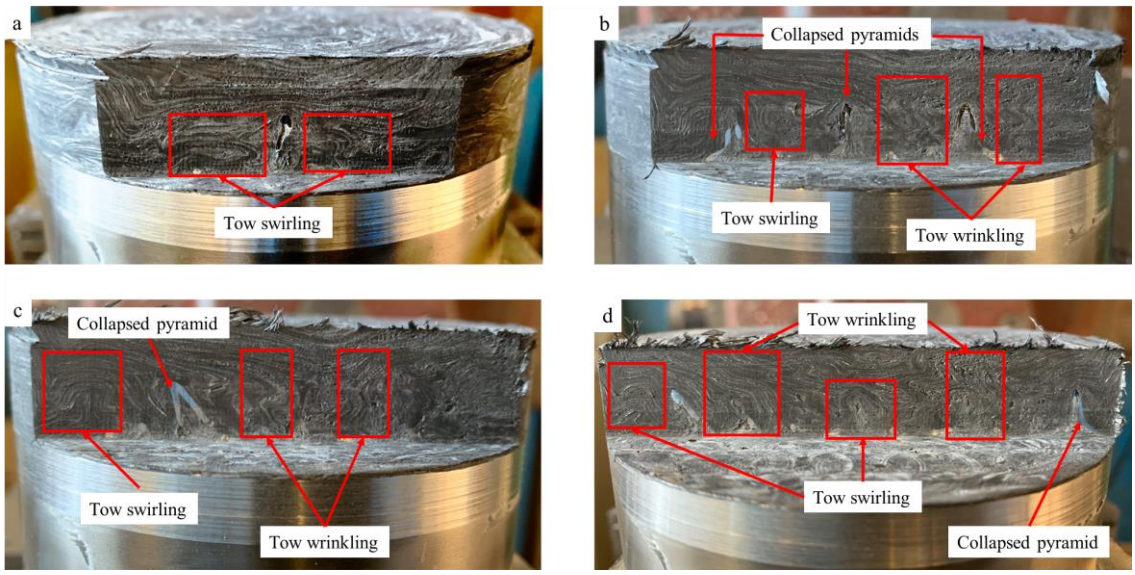

Figure 8: Infiltration results for Platform A (rough grid) - ASMC orthogonal to the interface

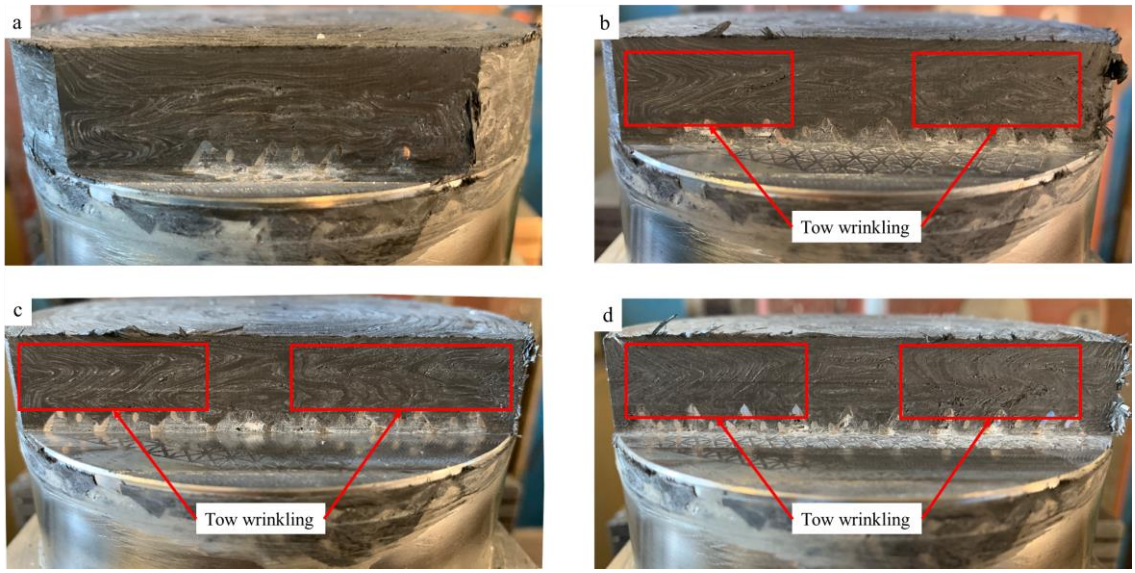

Figure 9: Infiltration results for Platform B (fine grid) - ASMC orthogonal to the interface

3.2. Mechanical Tests

Significant differences of mechanical properties were evidenced in the pull out tests depending on the preferential direction of the charge-constituting tows, as evidenced in Figure 10. Samples whose pyramids were embedded by a charge with tows parallel to the interface evidenced much lower strength than those penetrated by tows arranged perpendicularly to the interface, as a consequence of the defects already discussed in section 3.1. Moreover, the large dispersion of data for the parallel configuration led to a coefficient of variation (CVs) greater than 20% for all samples, further demonstrating the instability of the parallel configuration.

On the other hand, remarkable results are obtained for the orthogonal configuration, in particular for the small pyramids one, for which an average maximum load of 3554 N was found in contrast to the 1334 N of the big pyramid case and the 374 N of the reference sample. Also, for failure energy, a mean value of 2584 J for the small pyramid samples greatly exceeded the 895 Joules of the big pyramid ones and the 32 J of the reference samples.

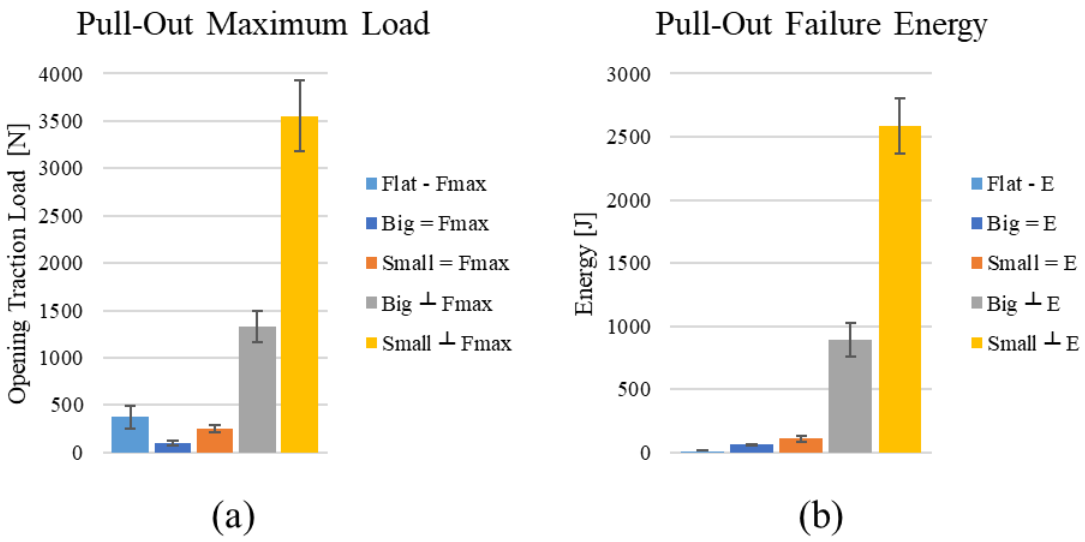

Figure 10: Summary of mechanical properties of the hybrid joints in the different tested configurations; 10a) Maximum Load; 10b) pullout failure energy

In Figure 11, the full pullout load-displacement curves for samples with orthogonal prepreg configuration are shown, evidencing excellent repeatability across all samples, with CVs values always lower than 14% in maximum pullout load and energy absorption except for the flat reference for which a CV of 25% was measured.

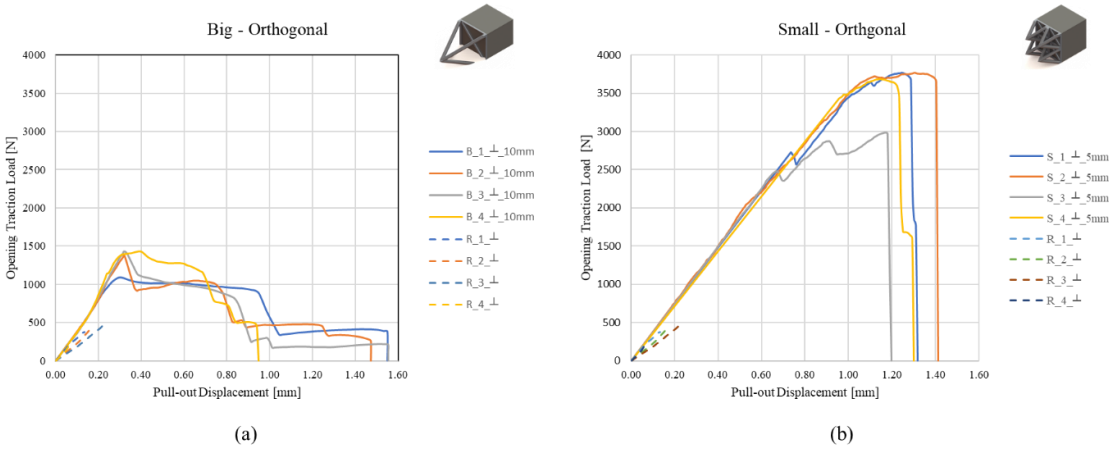

Figure 11: Load-displacement curves for both the orthogonal configurations. 11a) Big pyramids and reference samples; 11b) small pyramids and reference samples.

Samples with big pyramids showed a variable number of load drops during the test, often followed by wide “plateau” in which opening load was almost constant. This phenomenon, probably due to the progressive fracture of rods of the single embedded pyramid, provided a considerable increase in the energy absorbed. The maximum opening traction load was comparable (CV 12%) among samples with big pyramids, resulting in a hybrid joint that was 3.6 times stronger to the flat unstructured solution.

It must be noticed that, during tractioning, samples with big pyramids exhibited an increase in stiffness of about 1.5% from an average value of opening traction load equal to 640 N up to their first macroscopic failure. As demonstrated in section 3.1 and as reported in section S2 of supplementary information, the compression molding process induces a partial buckling of the big pyramids. During pullout, the deformed pyramid is supposed to interact with the composite material to recover its original shape partially, thus leading to an incremental stiffening effect on the specimens.

In samples with small pyramids, a linear behavior between traction load and displacement was detected up to the 79%-90% of the maximum load. Afterward, a marked plastic zone exists, which noticeably contributes to enhancing the absorbed energy of the joint: for this configuration, fracture energy was considerably higher than those measured in samples with big pyramids and in reference samples, respectively. Except for one sample, for which a progression of load drops is evidenced, few and less marked load drops were generally encountered for this configuration, with no change in the slope of the pullout load-displacement curves. Fracture analysis revealed that this behavior appeared in those samples in which voids and cavities were present. Maximum load was 2.7 times higher with respect to the big pyramids, and 9.5 times higher than the one measured on the flat reference. Pullout failure energy for this configuration was about three times higher than the one measured in samples with big pyramids and more than 80 times higher to the reference samples.

3.3. Analysis of the fractured surface and Morphological characterization

In the three types of samples infiltrated in the orthogonal configuration, different failure modes have been observed, and typical results of the stereomicroscopic analysis are shown in **Figure 12**.

On the metal side of the flat adherend (**Figure 12** a) only traces of resin are present, suggesting an adhesive failure mode of the samples. On the other hand, at the CFRP side, no traces of metal were found, thus confirming the hypothesis of merely adhesive fracture (**Figure 12** d).

In the case of samples with big pyramids (**Figure 12** b), only small regions with traces of resin are visible at the metal surface: close to rod ends and along with the edge features of the pyramid. On the CFRP side (**Figure 12** e), the resin is present almost everywhere, except for a limited number of small voids and cavities, probably due to

trapped air or gas formation during processing. The general scarcity of resin on the metal side, together with the near-full density of resin on the opposite side, suggests that an adhesive failure mode occurred at the metal-resin interface. At the same time, a marked plastic deformation of the corners of the pyramid is observable i.e., where the pyramids failed under the pullout traction load. From these observations, it can be argued that a large part of the failure energy exploited during the test is due to the progressive yielding of those regions.

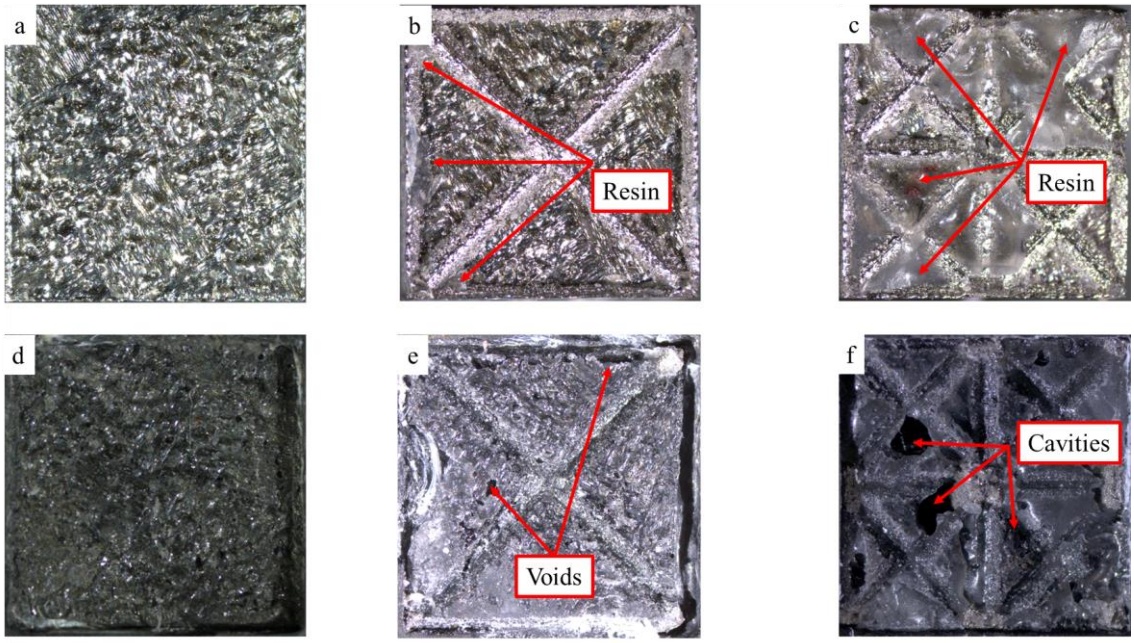

Figure 12: Fractured surfaces of samples infiltrated by the orthogonal configuration of tows. a), b) and c) metal side view, d), e) and f) CFRP side view; a) and d) reference (flat) sample; b) and e) big pyramid sample; c) and f) small pyramid sample;

In the sample with small pyramids (**Figure 12** c), the metal adherend appears to be uniformly covered by layers of resin with varying thickness, suggesting that the mode of fracture was typically cohesive, thus providing active participation of the interface to the overall joint resistance.

On the CFRP side (**Figure 12** f), the adherend shows some voids, probably due to a local lack of infiltration or trapped air [43] . Similar to what happens with big pyramids, also with small ones, there is evidence of extensive plastic deformation at the pyramids' bases, where the rods are connected to the bulk metal. It must be noticed, then, that the much larger number of corners in the small pyramid samples well explains the much higher maximum load of this configuration.

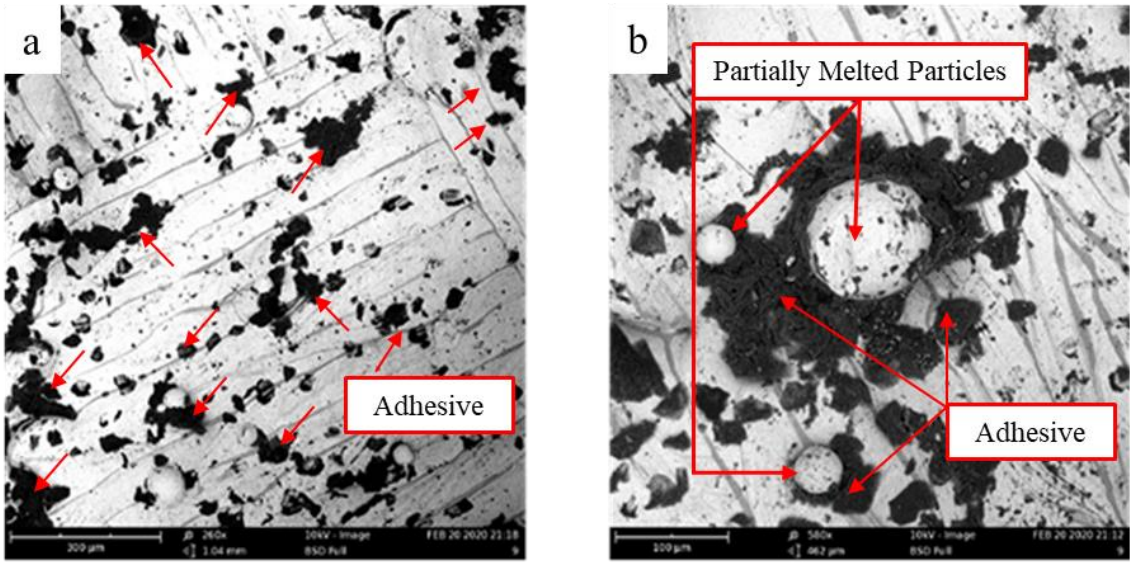

Figure 13: Magnification of fractured areas on the metal side for a) big pyramids, with a magnification of 260x, and b) big pyramids with a magnification of 560x

In samples with the big pyramids, and flat references as well, higher magnification analysis performed on the metal side of fractured surfaces (Figure 13) evidenced a mixed cohesive/adhesive fracture in the range 50-100 μm (Figure 13 a). Thanks to the unique morphology of the surface obtained by SLM process, a relatively high number of partially melted particles in the range 15-45μm were present. The resin was interestingly able to more strongly adhere, thanks to an interlocking mechanism, as evidenced in Figure 13 b and already reported by [44] for hybrid joints with titanium alloys.

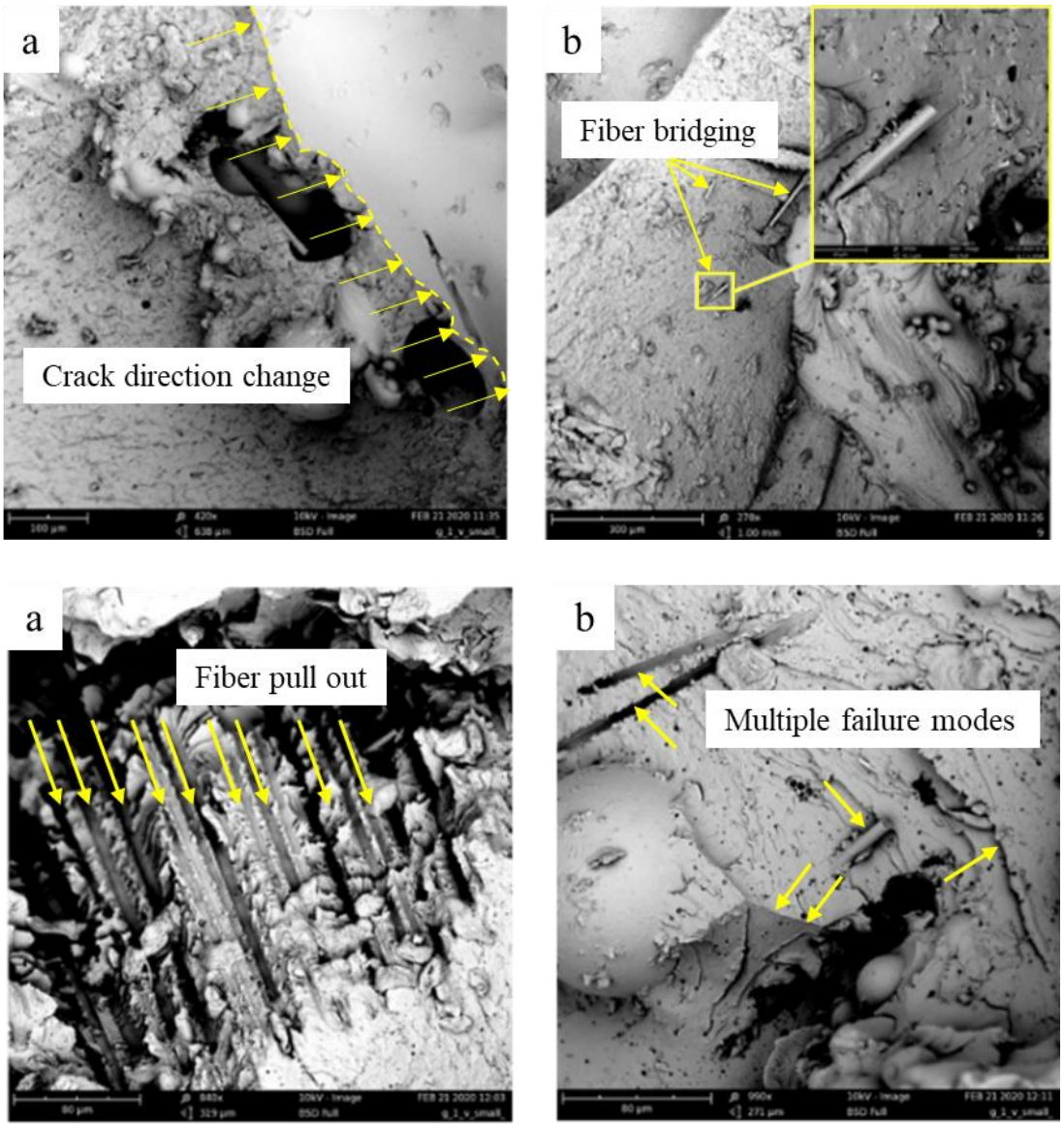

Figure 14: Fracture mechanisms in the small pyramids samples. a) crack direction changes b) fiber pullout c) fiber bridging and d) combination of previous mechanisms

In **Figure 14**, the fracture mechanisms present on the metal adherend of the small pyramid samples are shown. Here, the fully cohesive fracture that occurred during the pullout is evidenced by a mix of complex behaviors: the crack direction changes abruptly and frequently over the sample, as evidenced in **Figure 14** a, fiber pullout (**Figure 14** b) and fiber bridging (**Figure 14** c) can be observed in regions close to the connections between the metal base and the rods of the pyramids. The phenomena mentioned above generally coexist over the whole area of the metal adherend surface, as shown in **Figure 14** d. It must be underlined that the presence of fibers at the fracture surface is a clear sign of successful infiltration of fibers, and not only resin, into the lattice, even for the small pyramid structure.

4. Conclusions

An innovative technological solution for the manufacturing of high strength and high toughness metal-composite interface is here investigated, in which a 3DP printed cellular structure at the metal side is infiltrated by ASMC composite. The main findings are the following.

- The infiltration process is successful only when, in the bulk charge, the ASMC tows are oriented orthogonally to the lattice interface, in order to ease fiber displacement during the molding. In the orthogonal configuration, both lattices with small and big pyramids were successfully infiltrated.
- The lattice with big pyramids undergone some buckling under compression molding, evidencing a weak structure for the infiltration process; on the other hand, the lattice with small pyramids perfectly withstood the compression molding loads.
- When tested to pullout, the fracture always occurs at the lattice base in both lattices. The finer lattice failed under a load 2.66 times higher than, the rougher one, owing to the higher metal section provided to the pullout test. Moreover, the finer lattice promotes the resin fracture to occur by cohesive failure instead of adhesive one.
- As a general remark for the investigated technology, the hybrid samples with finer lattice could exhibit a pullout opening pressure force of about 3500 N and pullout energy of about 2500 J, which were respectively 10 and 80 times higher than the values obtained on the flat reference. Mechanical properties were found to be always consistent in this case.

5. Data availability

The raw/processed data required to reproduce these findings cannot be shared at this time as the data also forms part of an ongoing study.

Declaration of Competing Interest

The authors declare that they have no known competingfinancialinterests or personal relationships that could have appeared to influence the work reported in this paper.

References

[1] Goede M, Stehlin M, Rafflenbeul L, Kopp G, Beeh E. Super Light Car-lightweight construction thanks to a multi-material design and function integration. Eur Transp Res Rev 2009. https://doi.org/10.1007/s12544-008-0001-2.

[2] Gardiner G. Is the BMW 7 Series the future of autocomposites? Compos World 2016.

[3] Nehuis F, Kleemann S, Egede P, Vietor T, Herrmann C. Future trends in the development of vehicle bodies regarding lightweight and cost. Lect. Notes Mech. Eng., 2014. https://doi.org/10.1007/978-81-322-1871-5_3.

[4] Pervaiz M, Panthapulakkal S, KC B, Sain M, Tjong J. Emerging Trends in Automotive Lightweighting through Novel Composite Materials. Mater Sci Appl 2016. https://doi.org/10.4236/msa.2016.71004.

[5] Banea MD, Rosioara M, Carbas RJC, da Silva LFM. Multi-material adhesive joints for automotive industry. Compos Part B Eng 2018. https://doi.org/10.1016/j.compositesb.2018.06.009.

[6] Owens JFP, Lee-Sullivan P. Stiffness behaviour due to fracture in adhesively bonded composite-to-aluminum joints: I. Theoretical model. Int J Adhes Adhes 2000. https://doi.org/10.1016/S0143-7496(99)00013-5.

[7] Anyfantis KN, Tsouvalis NG. Loading and fracture response of CFRP-to-steel adhesively bonded joints with thick adherents - Part I: Experiments. Compos Struct 2013. https://doi.org/10.1016/j.compstruct.2012.08.060.

[8] Anyfantis KN, Tsouvalis NG. Loading and fracture response of CFRP-to-steel adhesively bonded joints with thick adherents - Part II: Numerical simulation. Compos Struct 2013. https://doi.org/10.1016/j.compstruct.2012.08.056.

[9] Ozel A, Yazici B, Akpinar S, Aydin MD, Temiz Ş. A study on the strength of adhesively bonded joints with different adherends. Compos Part B Eng 2014. https://doi.org/10.1016/j.compositesb.2014.03.001.

[10] Di Franco G, Fratini L, Pasta A. Analysis of the mechanical performance of hybrid (SPR/bonded) single-lap joints between CFRP panels and aluminum blanks. Int J Adhes Adhes 2013. https://doi.org/10.1016/j.ijadhadh.2012.10.008.

[11] Marannano G, Zuccarello B. Numerical experimental analysis of hybrid double lap aluminum-CFRP joints. Compos Part B Eng 2015. https://doi.org/10.1016/j.compositesb.2014.11.025.

[12] Korta J, Mlyniec A, Uhl T. Experimental and numerical study on the effect of humidity-temperature cycling on structural multi-material adhesive joints. Compos Part B Eng 2015. https://doi.org/10.1016/j.compositesb.2015.05.020.

[13] Povolo M, Raimondi L, Brugo TM, Pagani A, Comand D, Pirazzini L, et al. Design and manufacture of hybrid aluminum/composite co-cured tubes with viscoelastic interface layer. Procedia Struct. Integr., vol. 12, 2018. https://doi.org/10.1016/j.prostr.2018.11.095.

[14] Borsellino C, Di Bella G, Ruisi VF. Adhesive joining of aluminium AA6082: The effects of resin and surface treatment. Int J Adhes Adhes 2009.

https://doi.org/10.1016/j.ijadhadh.2008.01.002.

[15] Boutar Y, Naïmi S, Mezlini S, Ali MBS. Effect of surface treatment on the shear strength of aluminium adhesive single-lap joints for automotive applications. Int J Adhes Adhes 2016;67:38–43. https://doi.org/10.1016/j.ijadhadh.2015.12.023.

[16] Islam MS, Tong L, Falzon PJ. Influence of metal surface preparation on its surface profile, contact angle, surface energy and adhesion with glass fibre prepreg. Int J Adhes Adhes 2014. https://doi.org/10.1016/j.ijadhadh.2014.02.006.

[17] da Silva LFM, Carbas RJC, Critchlow GW, Figueiredo MAV, Brown K. Effect of material, geometry, surface treatment and environment on the shear strength of single lap joints. Int J Adhes Adhes 2009. https://doi.org/10.1016/j.ijadhadh.2009.02.012.

[18] Ucsnik S, Scheerer M, Zaremba S, Pahr DH. Experimental investigation of a novel hybrid metal-composite joining technology. Compos Part A Appl Sci Manuf 2010. https://doi.org/10.1016/j.compositesa.2009.11.003.

[19] Xiong W, Wang X, Dear JP, Blackman BRK. The effect of protrusion density on composite-metal joints with surfi-sculpt reinforcement. Compos Struct 2017. https://doi.org/10.1016/j.compstruct.2017.08.036.

[20] Smith F. Comeld - An innovation in composite to metal joining. Weld Cut 2005.

[21] Tu W, Wen PH, Hogg PJ, Guild FJ. Optimisation of the protrusion geometry in Comeld^{TM} joints. Compos Sci Technol 2011. https://doi.org/10.1016/j.compscitech.2011.02.001.

[22] Heimbs S, Nogueira AC, Hombergsmeier E, May M, Wolfrum J. Failure behaviour of composite T-joints with novel metallic arrow-pin reinforcement. Compos Struct 2014. https://doi.org/10.1016/j.compstruct.2013.11.022.

[23] Bisagni C, Furfari D, Pacchione M. Experimental investigation of reinforced bonded joints for composite laminates. J Compos Mater 2018. https://doi.org/10.1177/0021998317708021.

[24] Feraboli P, Peitso E, Deleo F, Cleveland T, Stickler PB. Characterization of prepreg-based discontinuous carbon fiber/epoxy systems. J Reinf Plast Compos 2009. https://doi.org/10.1177/0731684408088883.

[25] Selezneva M, Lessard L. Characterization of mechanical properties of randomly oriented strand thermoplastic composites. J Compos Mater 2016. https://doi.org/10.1177/0021998315613129.

[26] Grasso M, Colosimo BM. Process defects and in situ monitoring methods in metal powder bed fusion: A review. Meas Sci Technol 2017. https://doi.org/10.1088/1361-6501/aa5c4f.

[27] Everton SK, Hirsch M, Stavroulakis PI, Leach RK, Clare AT. Review of in-situ process monitoring and in-situ metrology for metal additive manufacturing. Mater Des 2016. https://doi.org/10.1016/j.matdes.2016.01.099.

[28] Grasso M, Laguzza V, Semeraro Q, Colosimo BM. In-Process Monitoring of Selective Laser Melting: Spatial Detection of Defects Via Image Data Analysis. J Manuf Sci Eng Trans ASME 2017. https://doi.org/10.1115/1.4034715.

[29] Martin Schoepf RHH. Method for producing a component assembly and component assembly. DE102015226742.3A, 2017.

[30] SUCH M, WARD C, POTTER K. Aligned Discontinuous Fibre Composites: A Short History. J Multifunct Compos 2014. https://doi.org/10.12783/issn.2168-4286/2/3/4.

[31] Visweswaraiah SB, Selezneva M, Lessard L, Hubert P. Mechanical characterisation and modelling of randomly oriented strand architecture and their hybrids – A general review. J Reinf Plast Compos 2018. https://doi.org/10.1177/0731684418754360.

[32] Du S, Guo ZS, Zhang B, Wu Z. Cure kinetics of epoxy resin used for advanced composites. Polym Int 2004. https://doi.org/10.1002/pi.1533.

[33] Wang J. PVT Properties of Polymers for Injection Molding. Some Crit. Issues Inject. Molding, 2012. https://doi.org/10.5772/35212.

[34] Wang J, Hopmann C, Schmitz M, Hohlweck T, Wipperfürth J. Modeling of pvT behavior of semi-crystalline polymer based on the two-domain Tait equation of state for injection molding. Mater Des 2019. https://doi.org/10.1016/j.matdes.2019.108149.

[35] Maconachie T, Leary M, Lozanovski B, Zhang X, Qian M, Faruque O, et al. SLM lattice structures: Properties, performance, applications and challenges. Mater Des 2019. https://doi.org/10.1016/j.matdes.2019.108137.

[36] Gibson, Lorna J and Ashby MF. Cellular solids: structure and properties. Cambridge university press; 1999.

[37] Deshpande VS, Fleck NA, Ashby MF. Effective properties of the octet-truss lattice material. J Mech Phys Solids 2001. https://doi.org/10.1016/S0022-5096(01)00010-2.

[38] Liverani E, Toschi S, Ceschini L, Fortunato A. Effect of selective laser melting (SLM) process parameters on microstructure and mechanical properties of 316L austenitic stainless steel. J Mater Process Technol 2017. https://doi.org/10.1016/j.jmatprotec.2017.05.042.

[39] Ashby MF, Bréchet YJM. Designing hybrid materials. Acta Mater 2003. https://doi.org/10.1016/S1359-6454(03)00441-5.

[40] Zhang Q, Lu T. Experimental and simulated compressive properties of work-hardened X-type lattice truss structures. Acta Mech Solida Sin 2012. https://doi.org/10.1016/S0894-9166(12)60012-3.

[41] Queheillalt DT, Carbajal G, Peterson GP, Wadley HNG. A multifunctional heat pipe sandwich panel structure. Int J Heat Mass Transf 2008. https://doi.org/10.1016/j.ijheatmasstransfer.2007.03.051.

[42] Tian J, Kim T, Lu TJ, Hodson HP, Queheillalt DT, Sypeck DJ, et al. The effects of topology upon fluid-flow and heat-transfer within cellular copper structures. Int J Heat Mass Transf 2004. https://doi.org/10.1016/j.ijheatmasstransfer.2004.02.010.

[43] Moeini Sedeh M, Khodadadi JM. Interface behavior and void formation during infiltration of liquids into porous structures. Int J Multiph Flow 2013.

https://doi.org/10.1016/j.ijmultiphaseflow.2013.07.002.

[44] Nguyen ATT, Brandt M, Orifici AC, Feih S. Hierarchical surface features for improved bonding and fracture toughness of metal-metal and metal-composite bonded joints. Int J Adhes Adhes 2016. https://doi.org/10.1016/j.ijadhadh.2015.12.005.

List of Figures